

THE UNIVERSITY OF NOTTINGHAM
SIR PETER MANSFIELD IMAGING CENTRE
SCHOOL OF PHYSICS AND ASTRONOMY

**Developing Techniques for Quantitative Renal Magnetic
Resonance Imaging**

Author:
Alexander James DANIEL MSci *Supervisor:*
Prof. Susan FRANCIS

5th February, 2021



Thesis submitted to the University of Nottingham for the degree of Doctor of Philosophy

Abstract

Science will happen, but this bit can be read by muggles on ‘tinterweb.

Contents

Abstract	i
Acknowledgments	vii
Abbreviations	viii
1 Introduction	1
1.1 Imaging in the Clinic	1
1.2 Clinical Motivation	2
1.3 Thesis Overview	6
1.4 References	8
2 Principles of Nuclear Magnetic Resonance Imaging	9
2.1 Source of the NMR Signal	10
2.1.1 Nuclear Spin	10
2.1.2 Application of an External Magnetic Field	11
2.1.3 Precession	12
2.1.4 Resonance	13
2.2 Relaxation and Contrast Mechanisms	15
2.2.1 Longitudinal Relaxation (T_1)	15
2.2.2 Transverse Relaxation (T_2 and T_2^*)	17
2.2.3 Dipole-Dipole Interactions	22
2.2.4 Diffusion Imaging	24
2.2.5 Optimisation of Tissue Contrast	25
2.3 Forming an Image	27
2.3.1 Signal Localisation	27

2.3.2	Image Acquisition Acceleration	34
2.3.3	Image Acquisition Schemes	36
2.4	Conclusion	42
2.5	References	43
3	Assessment of Renal T_2 Mapping Methods	47
3.1	Introduction	49
3.2	Methods	50
3.2.1	Data Acquisition	50
3.2.2	Post Processing	56
3.2.3	Assessment of Data	57
3.3	Results	60
3.3.1	Fitting Methods	60
3.3.2	Phantom Verification	63
3.3.3	In-Vivo	68
3.4	Discussion	70
3.5	Conclusion	73
3.6	Acknowledgements	74
3.7	References	75
4	Quantitative Methods to Measure Renal Oxygenation	81
4.1	Introduction	83
4.2	Methods	86
4.2.1	Susceptibility-Based Oximetry	86
4.2.2	T_2 Relaxation Under Spin Tagging	88
4.2.3	Inducing Changes in Oxygenation of Blood in the Renal Vein	94
4.3	Results and Discussion	96
4.3.1	Susceptibility-Based Oximetry	96
4.3.2	T_2 Relaxation Under Spin Tagging	98
4.4	Conclusions and Future Work	106
4.5	Acknowledgements	106
4.6	References	107

5 Automated Segmentation of Kidneys using Machine Learning	112
5.1 Introduction	114
5.2 Neural Networks for Image Segmentation	118
5.2.1 Artificial Neural Networks	118
5.2.2 Convolutional Neural Networks	121
5.3 Methods	124
5.3.1 MRI Data Acquisition	124
5.3.2 Manual Segmentation	125
5.3.3 Automated Segmentation Using a CNN Architecture .	125
5.3.4 Statistical Analysis	128
5.4 Results	130
5.4.1 Characteristics of the Training Cohort	130
5.4.2 Reducing Acquisition Time	131
5.4.3 Accuracy of Manual Segmentation	132
5.4.4 Network Testing	135
5.5 Discussion	142
5.5.1 Evaluation of Methodology	143
5.5.2 Future Directions	145
5.6 Conclusions	147
5.7 Acknowledgements	148
5.8 References	149
6 Ex-Vivo Renal MRI	155
6.1 Introduction	156
6.2 Methods	158
6.2.1 Sample Acquisition and Fixation	158
6.2.2 T_1 Mapping	158
6.2.3 T_2 Mapping	160
6.2.4 T_2^* Mapping	161
6.2.5 Apparent Diffusion Coefficient	162
6.2.6 Diffusion Tensor Imaging	162
6.2.7 Layer Based Analysis	164
6.3 Results and Discussion	167

6.3.1	Fixation and Protocol Development	167
6.3.2	Monitoring Changes in MR Parameters Post Fixation .	169
6.3.3	Comparing MR and Histological Measures in Aged Kidneys	174
6.4	Conclusions and Future Work	176
6.4.1	Protocol Validation on a Single Sample	177
6.4.2	Ex-Vivo Sample Coil	177
6.4.3	Human Organs	178
6.5	Acknowledgements	179
6.6	References	180
7	Conclusion	184

Todo list

 Make sure these are in the correct order	6
 add figure	71

Chapter 1

Introduction

1.1 Imaging in the Clinic

From April 2019 to March 2020, the United Kingdom's National Health Service (NHS) performed 45 million medical imaging procedures, of these 4 million were Magnetic Resonance Imaging (MRI) [1]. This technique can be used to produce high resolution volumetric images of the body with exquisite soft tissue contrast. Unlike other modalities, such as Computed Tomography (CT) and Positron Emission Tomography (PET), MRI uses non-ionising radiation, making it more suitable for longitudinal analysis of patient progression and research involving healthy volunteers.

The superior soft tissue contrast of MRI compared to CT meant it first found widespread clinical adoption in the field of neuroimaging. Here MRI has been used for diagnosis of neurological disorders, monitoring treatment progression and research into cognition. Many of the techniques honed in the brain, can be applied to the abdomen, where similar tissue properties can exploit the same techniques; albeit in a somewhat more challenging environment due to respiratory motion and a more inhomogeneous tissue structure. The kidneys are ideally suited to this translation as they have similar tissue properties to the brain and are highly dynamic organs.

1.2. Clinical Motivation

In addition to the acquisition of basic structural images, MRI can be used to collect quantitative information about the tissues being imaged. In this situation the numerical voxel values have physical significance, rather than simply representing signal intensity in arbitrary units [2]. Using quantitative MRI properties such as an organs oxygen consumption [3], perfusion [4], stiffness [5] and temperature [6] can be measured. Although many quantitative MRI techniques have been developed for the kidneys, there is still many methods where development, translation from the brain or standardisation with the wider renal community would be highly desirable.

1.2 Clinical Motivation

The kidneys are two bean shaped organs found in the abdomen, just below the rib cage, symmetrical about the spine. They participate in the control of bodily fluids by regulating the balance of electrolytes, excreting waste product of metabolism and excess water from blood into urine [7].

Kidneys are made up of units called nephrons, Figure 1.1, each of which contains a renal corpuscle and a tubule. The renal corpuscle itself is made up of a glomerulus and a Bowman capsule. The glomerulus is a cluster of capillaries that allow wastes and fluid to pass out of the blood stream into the Bowman capsule, while larger structures such as blood cells and proteins remain in the blood. The substances that passed through the glomerulus are moved to the tubules, each of which has blood vessels running alongside; these vessels reabsorb many of the important components of the blood such as the majority of the water, minerals and nutrients. The remaining fluids and waste in the tubules are collected in the ureter and removed from the body [8].

1.2. Clinical Motivation

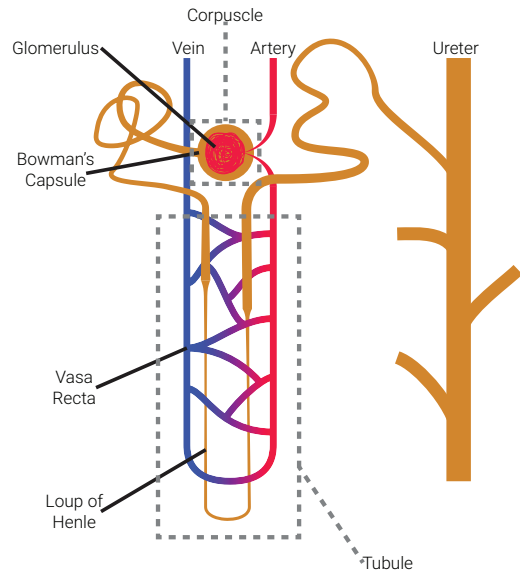


Figure 1.1: A schematic of the anatomy of a nephron.

Tissue in the kidney is separated into renal cortex, the outer portion of the kidney and renal medulla, the inner portion. The cortex contains the corpuscles with the tubules passing from the cortex to the medulla. Medullary tissue is compartmentalised into renal pyramids. Blood is supplied to the kidney via the renal artery, this branches into smaller vessels until it reaches the glomeruli then flows out via the renal vein. An overview of the gross anatomy of the kidney is shown in Figure 1.2.

1.2. Clinical Motivation

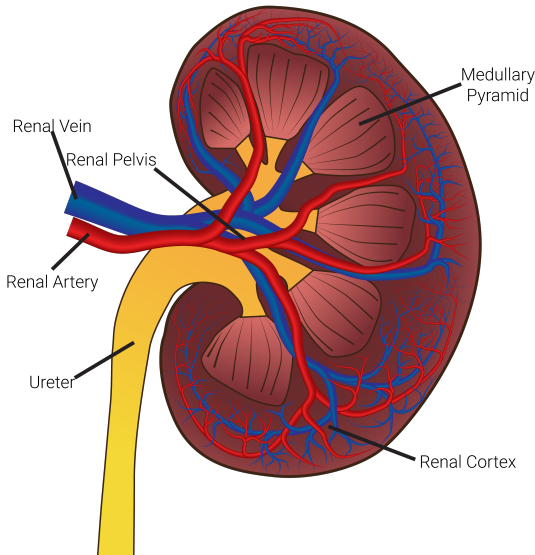


Figure 1.2: The gross anatomy of the kidney.

Due to their vital function in the body and the toxins they encounter as they perform their role, the kidneys are susceptible to problems. Chronic Kidney Disease (CKD) is the progressive destruction of the kidneys and therefore decrease in renal function. More quantitatively, CKD can be assessed clinically by Glomerular Filtration Rate (GFR), the rate at which fluid is filtered through the kidneys, with a value below $60 \text{ ml/min}/1.73\text{m}^2$ of body surface area being diagnostic or the presence of albumin, the main protein in blood plasma, in the patients urine [9–11]. Common causes of CKD are high blood pressure and diabetes as these damage the nephrons with high blood pressure also posing a risk to the blood vessels within the kidney. Renal tissue is highly vascularised and as such, the risks associated with high blood pressure are especially prevalent in the kidneys. An estimated 5–11% of the global population suffer from CKD [12–16] making it a significant public health concern. Late referral of renal disorders results in an increase in mortality rate and treatment costs [17–19]. Given that in 2013/2014 renal services cost the NHS £586 million [20] there are clear health and economic advantages to an early diagnosis and improved treatment of CKD. This can either be achieved via directly aiding diagnosis i.e. developing tools used on to assess patients condition and tailor treatment, or via improving understanding of CKD leading

1.3. Thesis Overview

to an earlier, more accurate diagnosis using existing techniques and thus more personalised medicine.

The current methods available to study CKD are not ideal for a variety of reasons. Histological samples are the gold standard for studying renal tissue however collecting them is an invasive process and as such they are not suitable for monitoring the progress of a patient's condition on a regular basis. This coupled with the fact that a small sample is not representative of the entirety of both kidneys means that this method has large drawbacks. Ultrasound can be used to gather structural information about the kidneys non-invasively, however, it suffers from low spatial resolution and the images being difficult to interpret [21]. The most common method of diagnosis is to estimate GFR from the creatinine content in a blood sample however this measure does not allow for the individual assessment of each kidney and is an indirect measure of kidney tissue damage.

MRI is an ideal modality for the study of kidney disease due to its non-ionising, non-invasive and quantitative nature. A current research interest at the Sir Peter Mansfield Imaging Centre (SPMIC) is the use of a multi-parametric quantitative renal MRI protocol to assess and predict CKD [22, 23]. This protocol is used to measure multiple quantitative properties of the kidneys with relative increases/decreases between measurements functioning as biomarkers and therefore indications of CKD progression. The implementation of new quantitative renal imaging methods can improve this protocol, thus increasing its clinical application. In addition to the CKD paradigm, we wish to apply these methods ex-vivo, both to allow a more direct comparison with current gold standards, such as histopathology, and to aid with assessment of renal allograft viability.

1.3 Thesis Overview

1.3. Thesis Overview

Chapter 2 provides the theoretical framework of Nuclear Magnetic Resonance (NMR) and MRI. A detailed description is given of the origin of the measured signal, processes that give rise to contrast between tissues and the methods of image formation.

Chapter 3 explores T_2 mapping within the kidneys. There is little consensus as to which method should be used within the kidneys [24], thus leading to inconsistent values quoted between studies [25]. Here multiple methods from the literature are compared assessing their quantitative accuracy and image quality in phantoms before five subjects are scanned to assess the methods in-vivo.

Chapter 4 aims to translate methods for measuring blood oxygenation from vessels in the brain to use within the kidneys. Focusing on Susceptibility Based Oximetry (SBO) [26] and T_2 Relaxation Under Spin Tagging (TRUST) [27] this chapter optimises the methods for use in the abdomen, verifying the modifications in the brain, then carries out an oxygen challenge in-vivo to measure changes in oxygen saturation within the renal vein.

Chapter 5 describes the development of a fully automated method to segment the kidneys from MRI data. Defining renal masks is an important, yet time consuming, aspect of many studies. The masks can be used to calculate Total Kidney Volume (TKV) or to inform downstream processing. Here a Convolutional Neural Network (CNN) is developed to segment the kidneys from T_2 weighted Half-Fourier Single-shot Turbo spin Echo (HASTE) images. Software is developed to provide an executable that allows anyone to segment the kidneys in a few seconds on regular office hardware.

Chapter 6 develops methods for scanning kidneys ex-vivo. The clinical gold standard for diagnosis of renal pathologies is biopsy followed by histological analysis. Comparison between this gold standard and recently developed quantitative MRI techniques is vital for clinical translation. Here a pipeline for multi-parametric imaging of the same kidney in-vivo, ex-vivo followed by histology is developed.

1.3. Thesis Overview

Chapter 7 concludes the thesis, highlighting key results and their current applications. It also provides an overview as to future research directions and how the methods developed could be applied to new paradigms or expanded upon.

1.4 References

1. *Diagnostic Imaging Dataset Annual Statistical Release 2019/20* <https://www.england.nhs.uk/statistics/statistical-work-areas/diagnostic-imaging-dataset/diagnostic-imaging-dataset-2019-20-data/> (2021).
2. Tofts, P. *Quantitative MRI of the Brain: Measuring Changes Caused by Disease* 688 pp. ISBN: 978-0-470-84721-3. Google Books: RbFrAAAAMAAJ (Wiley, 2003).
3. Zhang, J. *et al.* Quantitative Mapping of Cerebral Metabolic Rate of Oxygen (CMRO₂) Using Quantitative Susceptibility Mapping (QSM). *Magnetic Resonance in Medicine* **74**, 945–952. ISSN: 1522-2594 (1st Oct. 2015).
4. Karger, N. *et al.* Quantitation of Renal Perfusion Using Arterial Spin Labeling with FAIR-UFLARE. *Magnetic Resonance Imaging* **18**, 641–647. ISSN: 0730-725X (1st July 2000).
5. Mariappan, Y. K., Glaser, K. J. & Ehman, R. L. MAGNETIC RESONANCE ELASTOGRAPHY: A REVIEW. *Clinical anatomy (New York, N.Y.)* **23**, 497–511. ISSN: 0897-3806 (July 2010).
6. Yuan, J., Mei, C.-S., Panych, L. P., McDannold, N. J. & Madore, B. Towards Fast and Accurate Temperature Mapping with Proton Resonance Frequency-Based MR Thermometry. *Quantitative Imaging in Medicine and Surgery* **2**, 212–232. ISSN: 2223-4306, 2223-4292 (Mar. 2012).
7. Lote, C. J. *Principles of Renal Physiology* 255 pp. ISBN: 978-94-011-4086-7. Google Books: at6LBQAAQBAJ (Springer Science & Business Media, 6th Dec. 2012).
8. Hall, J. E. *Guyton and Hall Textbook of Medical Physiology* 1171 pp. ISBN: 978-1-4557-7005-2. Google Books: 3sWNCgAAQBAJ (Elsevier Health Sciences, 20th May 2015).
9. Stevens, L. A., Coresh, J., Greene, T. & Levey, A. S. Assessing Kidney Function — Measured and Estimated Glomerular Filtration Rate. *New England Journal of Medicine* **354**, 2473–2483. ISSN: 0028-4793 (8th June 2006).

1.4. References

10. Farrugia, A. Albumin Usage in Clinical Medicine: Tradition or Therapeutic? *Transfusion Medicine Reviews* **24**, 53–63. issn: 0887-7963, 1532-9496 (1st Jan. 2010).
11. Pruijm, M., Milani, B. & Burnier, M. Blood Oxygenation Level-Dependent MRI to Assess Renal Oxygenation in Renal Diseases: Progresses and Challenges. *Frontiers in Physiology* **7**. issn: 1664-042X. pmid: 28105019 (5th Jan. 2017).
12. Coresh, J., Astor, B. C., Greene, T., Eknayan, G. & Levey, A. S. Prevalence of Chronic Kidney Disease and Decreased Kidney Function in the Adult US Population: Third National Health and Nutrition Examination Survey. *American Journal of Kidney Diseases: The Official Journal of the National Kidney Foundation* **41**, 1–12. issn: 1523-6838 (Jan. 2003).
13. De Lusignan, S. *et al.* Identifying Patients with Chronic Kidney Disease from General Practice Computer Records. *Family Practice* **22**, 234–241. issn: 0263-2136 (1st June 2005).
14. Drey, N., Roderick, P., Mullee, M. & Rogerson, M. A Population-Based Study of the Incidence and Outcomes of Diagnosed Chronic Kidney Disease. *American Journal of Kidney Diseases* **42**, 677–684. issn: 0272-6386 (1st Oct. 2003).
15. Amato, D. *et al.* Prevalence of Chronic Kidney Disease in an Urban Mexican Population. *Kidney International* **68**, S11–S17. issn: 0085-2538 (1st Aug. 2005).
16. Chadban, S. J. *et al.* Prevalence of Kidney Damage in Australian Adults: The AusDiab Kidney Study. *Journal of the American Society of Nephrology* **14**, S131–S138. issn: 1046-6673, 1533-8450 (suppl 2 1st July 2003).
17. Jungers, P. *et al.* Late Referral to Maintenance Dialysis: Detrimental Consequences. *Nephrology Dialysis Transplantation* **8**, 1089–1093. issn: 0931-0509 (1st Jan. 1993).
18. Sesso, R. & Belasco, A. G. Late Diagnosis of Chronic Renal Failure and Mortality on Maintenance Dialysis. *Nephrology Dialysis Transplantation* **11**, 2417–2420. issn: 0931-0509 (1st Dec. 1996).

1.4. References

19. Klebe, B. *et al.* The Cost of Implementing UK Guidelines for the Management of Chronic Kidney Disease. *Nephrology Dialysis Transplantation* **22**, 2504–2512. issn: 0931-0509 (1st Sept. 2007).
20. Precious, K. *NHS England » Programme Budgeting* <https://www.england.nhs.uk/resources/resources-for-ccgs/prog-budgeting/> (2017).
21. Hansen, K. L., Nielsen, M. B. & Ewertsen, C. Ultrasonography of the Kidney: A Pictorial Review. *Diagnostics* **6**. issn: 2075-4418. pmid: 26838799 (23rd Dec. 2015).
22. Cox, E. F. *et al.* Multiparametric Renal Magnetic Resonance Imaging: Validation, Interventions, and Alterations in Chronic Kidney Disease. *Frontiers in Physiology* **8**. issn: 1664-042X (2017).
23. Buchanan, C. E. *et al.* Quantitative Assessment of Renal Structural and Functional Changes in Chronic Kidney Disease Using Multi-Parametric Magnetic Resonance Imaging. *Nephrology Dialysis Transplantation* (29th June 2019).
24. Dekkers, I. A. *et al.* Consensus-Based Technical Recommendations for Clinical Translation of Renal T1 and T2 Mapping MRI. *Magnetic Resonance Materials in Physics, Biology and Medicine*. issn: 1352-8661 (22nd Nov. 2019).
25. Wolf, M. *et al.* Magnetic Resonance Imaging T1- and T2-Mapping to Assess Renal Structure and Function: A Systematic Review and Statement Paper. *Nephrology Dialysis Transplantation* **33**, ii41–ii50. issn: 0931-0509 (suppl_2 1st Sept. 2018).
26. Jain, V., Langham, M. C. & Wehrli, F. W. MRI Estimation of Global Brain Oxygen Consumption Rate. *Journal of Cerebral Blood Flow & Metabolism* **30**, 1598–1607. issn: 0271-678X (1st Sept. 2010).
27. Lu, H. & Ge, Y. Quantitative Evaluation of Oxygenation in Venous Vessels Using T2-Relaxation-Under-Spin-Tagging MRI. *Magnetic Resonance in Medicine* **60**, 357–363. issn: 1522-2594 (1st Aug. 2008).

Chapter 2

Principles of Nuclear Magnetic Resonance Imaging

Abstract

This chapter outlines the theoretical framework behind Nuclear Magnetic Resonance (NMR) and Magnetic Resonance Imaging (MRI). Beginning with an overview of nuclear spin and resonance, the origin of the signal measured in Nuclear Magnetic Resonance (NMR) is explained. The processes responsible for variations within signals such as relaxation mechanisms is then outlined in addition to techniques used to measure these different signals. Finally an overview of the process by which the signals can be used to form images is given, covering concepts such as spacial localisation, image acquisition schemes and acceleration methods.

2.1 Source of the NMR Signal

2.1.1 Nuclear Spin

The NMR signal arises from the interaction between the atomic nucleus and an external magnetic field. These atomic nuclei possess intrinsic properties, mass (m), charge (q) and spin (I). Spin is a quantum mechanical property and as such, can only take values of half integers or integers. Nuclear spin is dictated by the sum of the constituent particles of the nucleus, protons and neutrons, each of which possesses their own spin of either $1/2$ or $-1/2$ respectively. The additive nature of nuclear spin means that pairs of nucleons can cancel out leaving the nucleus with zero net spin, this happens when the nucleus contains an even number of protons and neutrons. If the nucleus contains an odd number of both protons and neutrons, it will have a positive integer nuclear spin whereas if the nucleus has an odd number of protons or neutrons, it will have a half integer spin.

The spin angular momentum, \mathbf{J} of a nucleus of spin I is given by

$$|\mathbf{J}| = \hbar\sqrt{I(I+1)} \quad (2.1)$$

where \hbar is the reduced Plank's constant, $h/2\pi$. As the nucleus is charged and rotating, it gives rise to a current and therefore a magnetic moment μ ,

$$\mu = \gamma \mathbf{J} \quad (2.2)$$

where γ is the gyromagnetic ratio for the nucleus, a constant which depends on the charge and mass of the nucleus. Table 2.1 shows the gyromagnetic ratio (γ) and nuclear spin (I) of common NMR sensitive isotopes [1–3]. Due to its high gyromagnetic ratio, compared to other nuclei used for NMR, and relative abundance in the body, ^1H , a single proton, is most commonly used for Magnetic Resonance Imaging (MRI).

2.1. Source of the NMR Signal

Isotope	Spin	γ (MHzT $^{-1}$)	Sensitivity Relative to ^1H
^1H	$^{1/2}$	42.58	1
^2H	1	6.54	0.0097
^{13}C	$^{1/2}$	10.71	0.016
^{19}F	$^{1/2}$	40.05	0.83
^{23}Na	$^{3/2}$	11.27	0.093
^{31}P	$^{1/2}$	17.25	0.066

Table 2.1: Common NMR isotopes, their nuclear spin, gyromagnetic ratio and sensitivity, relative to ^1H .

2.1.2 Application of an External Magnetic Field

If we consider the hydrogen nuclei in a sample of tissue, the number of possible eigenstates for a nucleus of nuclear spin I is $(2I + 1)$. This means that for the ^1H nuclei in our sample, where $I = 1/2$, we can observe two possible eigenstates, $|+1/2\rangle$ and $|{-1/2}\rangle$ often written as $|\uparrow\rangle$ and $|\downarrow\rangle$. In the absence of an external magnetic field, these states are degenerate as they have the same energy, however, if we move our sample into a static external magnetic field along the z -axis, B_0 , the energy levels separate.

The z -component of the magnetic moment is defined by,

$$\mu_z = \gamma \hbar m_I \quad (2.3)$$

where m_I are the possible spin quantum numbers of the nucleus. For our proton system with spin $1/2$, μ_z is given by

$$\mu_z = \pm \frac{1}{2} \gamma \hbar. \quad (2.4)$$

The spins can either be aligned parallel to the external magnetic field in the lower energy of the two eigenstates, also known as spin up; or anti-parallel to the magnetic field in the higher energy eigenstate, spin down. The energy

2.1. Source of the NMR Signal

difference between these two eigenstates is given by,

$$\Delta E = \gamma \hbar B_0. \quad (2.5)$$

For an ensemble of spins in an external magnetic field, there will be an imbalance between the populations of each state with more spins occupying the lower of the two energy states. The net magnetisation of the sample is simply the sum of the constituent spins and as such, the application of an external magnetic field leads to the sample gaining a net magnetisation vector aligned with B_0 . This effect is very small, the magnitude of the imbalance between eigenstates can be derived from Boltzmann statistics and is given by,

$$\frac{N_\uparrow}{N_\downarrow} = \exp\left(\frac{\Delta E}{k_B T}\right), \quad (2.6)$$

where N_\downarrow and N_\uparrow are the number of spins aligned with and against B_0 respectively, k_B is Boltzmann's constant and T is the temperature of the system. This means that for a sample of biological tissue at body temperature in a 3T magnetic field, the population difference is very small at approximately three parts per million. Although this measurable proportion is very small, it can be detected due to the high density of protons in the tissue. The signal can also be increased by the application of a stronger B_0 .

2.1.3 Precession

Classically, if a magnetic moment, M , is placed into an external magnetic field, B , it will experience a torque, τ , proportional to change in angular momentum and thus induce a rotation.

$$\mathbf{M} \times \mathbf{B} = \frac{d\mathbf{J}}{dt} = \boldsymbol{\tau} \quad (2.7)$$

2.1. Source of the NMR Signal

From (2.2) the quantum equivalent of (2.7) is the standard form of the Bloch equation [4],

$$\frac{d\mu}{dt} = \gamma \mu \times \mathbf{B} \quad (2.8)$$

This equation states that if the magnetic moment, μ is not aligned with the external magnetic field, \mathbf{B} , it will precess about \mathbf{B} . The frequency of this precession, ω_0 is known as the Larmor frequency and is given by substituting Bohr's frequency condition of the Planck relation ($\Delta E = \hbar\omega$) into (2.5),

$$\omega_0 = \gamma B_0, \quad (2.9)$$

Nuclei with a positive gyromagnetic ratio precess clockwise, whereas nuclei (and the electron) with a negative gyromagnetic ratio precess anti-clockwise. For a proton in a 3T magnetic field, the Larmor frequency is 128 MHz.

2.1.4 Resonance

Resonance is the process of energy transfer into a system by the application of energy at the natural frequency of the system. In the case of NMR this is the application of an Radio Frequency (RF) pulse, also known as B_1 field, near the Larmor frequency. Before the RF pulse is applied, the spins are at equilibrium, aligned with B_0 . Upon the application of a B_1 field close to the Larmor frequency of the target nucleus and perpendicular to B_0 , the spins aligned with B_0 will be displaced from equilibrium and thus precession is induced. The longer the B_1 field is applied, the more the net magnetisation vector is displaced, or tipped, away from B_0 , this allows arbitrary flip angles, α , to be achieved, (2.10).

$$\alpha = \int_0^T \gamma B_1(t) dt \quad (2.10)$$

In addition to displacing the spins, the B_1 field also induces phase coherence within the ensemble making up the net magnetisation vector. When considering the effects of RF pulses, it can often be simpler to imagine the system from

2.1. Source of the NMR Signal

a reference frame rotating about the z -axis at the Larmor frequency. This has the effect of making B_1 stationary along the x -axis. Figure 2.1 shows the evolution of a spin in both the laboratory and rotating frame after the application of a 90° RF pulse. In both figures the spin is tipped into the transverse plane, M_{xy} .

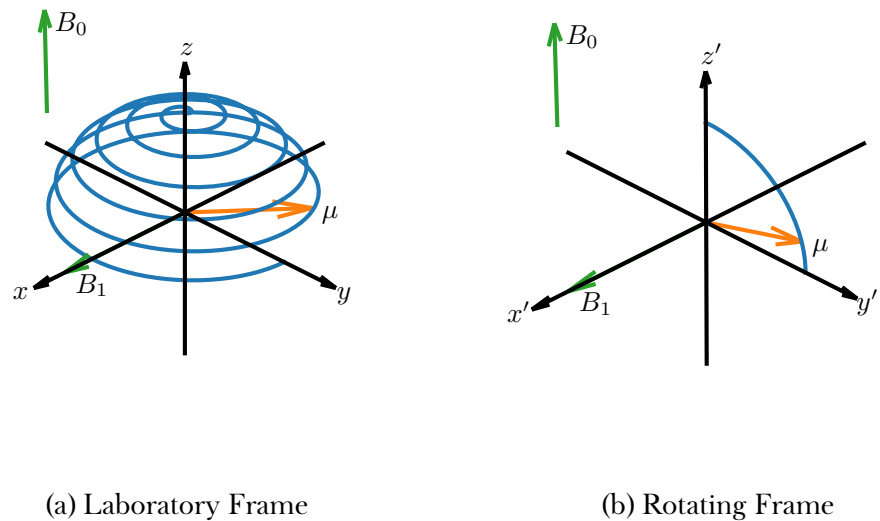


Figure 2.1: The laboratory frame of reference shows the procession of the spin about B_0 while in the rotating frame, the spin simply rotates about the x' -axis

2.2 Relaxation and Contrast Mechanisms

If disturbed from equilibrium by an RF pulse, the net magnetisation vector will not remain in this new state ad infinitum, instead, once the RF pulse has finished, it will transition back to its equilibrium state in a process known as relaxation. The time constants characterising the relaxation process vary depending on the environment the spins are in and as such, can vary between different biological tissues. These relaxation constants are the principle source of contrast in MRI. Mathematically, this relaxation is described by the full form of the Bloch equation, (2.11).

$$\frac{d\mathbf{M}}{dt} = \gamma(\mathbf{M} \times \mathbf{B}) - \frac{(M_z - M_0)}{T_1}\hat{\mathbf{z}} - \frac{M_x\hat{\mathbf{x}} + M_y\hat{\mathbf{y}}}{T_2} \quad (2.11)$$

2.2.1 Longitudinal Relaxation (T_1)

Upon excitation, energy is exchanged between the spin system and the surrounding environment. The result of this energy exchange is that the energy of the spin system decreases and the longitudinal magnetisation exponentially decays to its equilibrium position. The time constant of this exponential decay returning to equilibrium, M_0 , is known as the longitudinal relaxation time or T_1 and is dictated by the efficiency of energy transfer between the spin system and the surrounding lattice, hence its historical name, spin-lattice relaxation.

The efficiency of this energy transfer is primarily dictated by the motion of the surrounding lattice. As nearby molecules undergo rotation they cause variations in the local magnetic field. If these fluctuations are at a similar frequency to the Larmor frequency then energy transfer via dipole-dipole interactions will be relatively efficient. The rate of energy transfer can also be increased if the molecules are more closely coupled for example, tissues with a lower molecular mobility tend to have a shorter T_1 than those with a high molecular mobility.

Measuring T_1

The longitudinal component of the Bloch equation, (2.11), is given by (2.12).

$$\frac{d\mathbf{M}_z}{dt} = -\frac{(M_z - M_0)}{T_1} \quad (2.12)$$

Solving this equation for M_z gives,

$$M_z = M_0 \left[1 - \exp \left(-\frac{t}{T_1} \right) \right] + M_z(0) \exp \left(-\frac{t}{T_1} \right) \quad (2.13)$$

The gold standard method for quantification of T_1 is the inversion recovery pulse sequence in which a 180° pulse is used to fully invert the magnetisation, such that $M_z(0) = -M_0$ and as such (2.13) reduces to,

$$M_z = M_0 \left[1 - 2 \exp \left(-\frac{t}{T_1} \right) \right]. \quad (2.14)$$

To measure T_1 , the experiment is repeated multiple times, with measurements of M_z taken at different times after the 180° inversion pulse, Inversion Time (TI). The magnetisation must have fully recovered to M_0 between each inversion pulse, as such the minimum time between inversions, Repetition Time (TR) is five times T_1 . Curve fitting can then be used to estimate M_0 and T_1 , Figure 2.2. This method is expanded upon when it is used in Chapter 6.

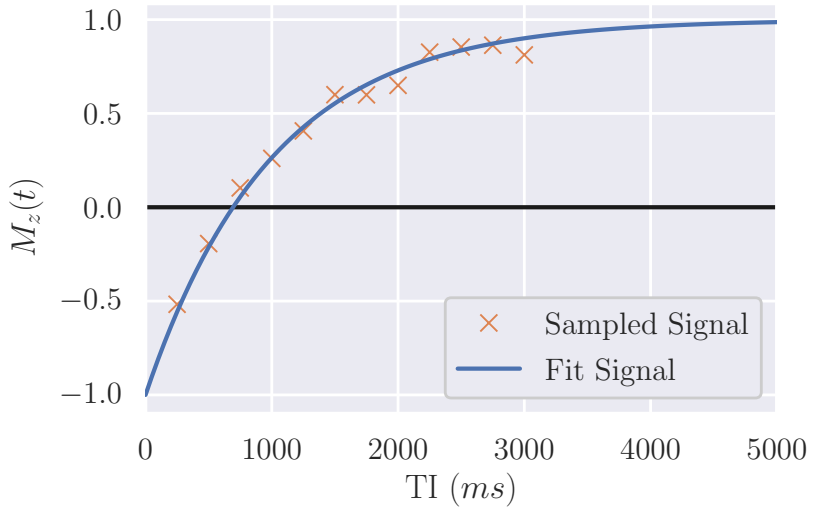


Figure 2.2: The longitudinal magnetisation for a sample of $T_1 = 1000$ ms in an inversion recovery experiment. The experiment was repeated with inversion times from 250 ms to 3000 ms in 250 ms steps.

2.2.2 Transverse Relaxation (T_2 and T_2^*)

Upon the application of a 90° RF pulse, the net magnetisation vector has tipped in the y' direction resulting in phase coherence and creating transverse magnetisation, $M_{x'y'}$. The spins then precess about the z -axis at their Larmor frequency, dictated by the magnetic field they are in. This magnetic field is not perfectly homogenous over the whole ensemble though, random dipole-dipole interaction with neighbouring spins produce short-lived fluctuations in the local magnetic field and thus the Larmor frequency of each spin varies. As the spins precess at different frequencies, they de-phase, resulting in the transverse magnetisation decaying to zero as phase coherence is lost. This mechanism is driven by energy transfer between the spins within the system so is sometimes termed, spin-spin relaxation. The rate at which this loss of phase coherence due to spin-spin interactions occurs is characterised by the time constant T_2 .

The local magnetic field is not just influenced by spin-spin interactions. Local inhomogeneities in the static B_0 field can be caused by susceptibility

differences within the sample and hardware imperfections. These B_0 inhomogeneities result in additional perturbation to the local magnetic field and therefore results in additional de-phasing of the system. The rate at which this de-phasing due to static B_0 inhomogeneities occurs is characterised by the time constant T'_2 . The measured decay in transverse magnetisation is therefore dictated by T_2^* , which is related to T_2 and T'_2 by

$$\frac{1}{T_2^*} = \frac{1}{T_2} + \frac{1}{T'_2}. \quad (2.15)$$

Measuring T_2 and T_2^*

The transverse component of the Bloch equation, (2.11), is given by (2.16).

$$\frac{dM_{xy}}{dt} = -\frac{M_{xy}}{T_2} \quad (2.16)$$

Solving the differential equation for M_{xy} with respect to t gives,

$$M_{xy}(t) = M_{xy}(0) \exp\left(-\frac{t}{T_2}\right), \quad (2.17)$$

It should be noted that (2.17) is an idealised equation and thus does not include static field inhomogeneities that contribute to T'_2 and thus the magnetisation of a real signal will decay with T_2^* .

After a 90° RF pulse the envelope of the signal will decay with T_2^* , known as an Free Induction Decay (FID). As such, by measuring the amplitude of the signal at different time points, t , the decay can be sampled and fit to estimate T_2^* .

Spin Echoes

To measure T_2 , rather than T_2^* , the effects of static B_0 inhomogeneities that lead to T'_2 must be negated. Because the processes driving the de-phasing that lead to T'_2 are constant over time, the refocussing effects of a Spin Echo (SE)

2.2. Relaxation and Contrast Mechanisms

sequence, outlined in Figure 2.3, can be utilised to reform this de-phasing component. In a SE sequence, an initial 90° excitation pulse shifts M into the transverse plane and induces phase coherence, Figure 2.4a. T_2^* effects will then cause some spins to precess quickly and others more slowly and thus dephase with T_2^* , Figure 2.4b. At time, Echo Time (TE)/2, later a 180° pulse is used to flip the spin ensemble, reversing the phase shift meaning those spins that had accrued the largest positive phase shift will now have the largest negative phase shift and vice versa, Figure 2.4c. Because the B_0 inhomogeneities that lead to T_2' are static, they will still be acting to the same degree on each spin. This leads to an echo forming at $t = \text{TE}$ as those spins with the highest Larmor frequency, and largest negative phase shift, refocus or “catch up” with those spins with a lower Larmor frequency, Figure 2.4d. The processes leading to T_2 are not constant over time and as such are not refocussed by the 180° pulse, hence the echo in Figure 2.4d is not perfectly refocussed and the signal will be attenuated at a rate dictated by T_2 .

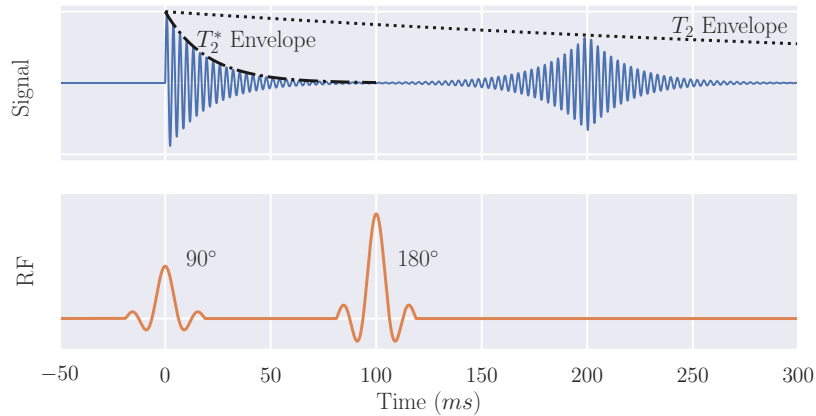


Figure 2.3: The signal produced in a spin-echo sequence used to measure T_2 . This sequence has a TE of 200 ms.

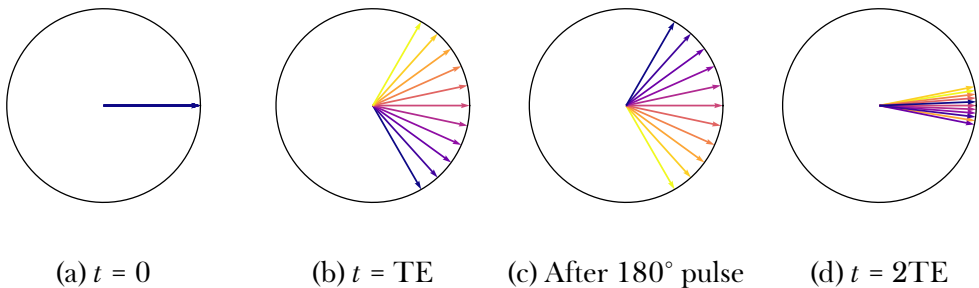


Figure 2.4: Spins evolving in a spin echo sequence showing the de-phasing, (b), refocusing pulse, (c), and subsequent refocusing, (d).

By repeating this sequence over a range of TE the T_2 curve can be samples and fit to (2.17) to estimate T_2 and M_{xy0} . The SE sequence is the most basic form of T_2 mapping, more methods are explored and compared in Chapter 3.

Gradient Echoes

Echoes can be generated via another mechanism, the Gradient Echo (GE). In addition to the homogenous B_0 field and RF fields encountered thus far, MRI scanners can produce additional fields known as gradients. These switchable fields can induce linearly varying spatially dependent magnetic fields to perturb B_0 . They are used for image formation, explained in Section 2.3 but can also be used to form an echo. The GE pulse sequence uses a single 90° RF excitation pulse to tip the net magnetisation vector into the transverse plane. A gradient is then applied to the sample causing areas of higher field to dephase quickly whereas areas with a relatively lower field will de-phase slower. At time $TE/2$ the polarity of the gradient is reversed thus causing the spins to refocus and an echo to be formed at time TE . An overview of the sequence is shown in Figure 2.5.

2.2. Relaxation and Contrast Mechanisms

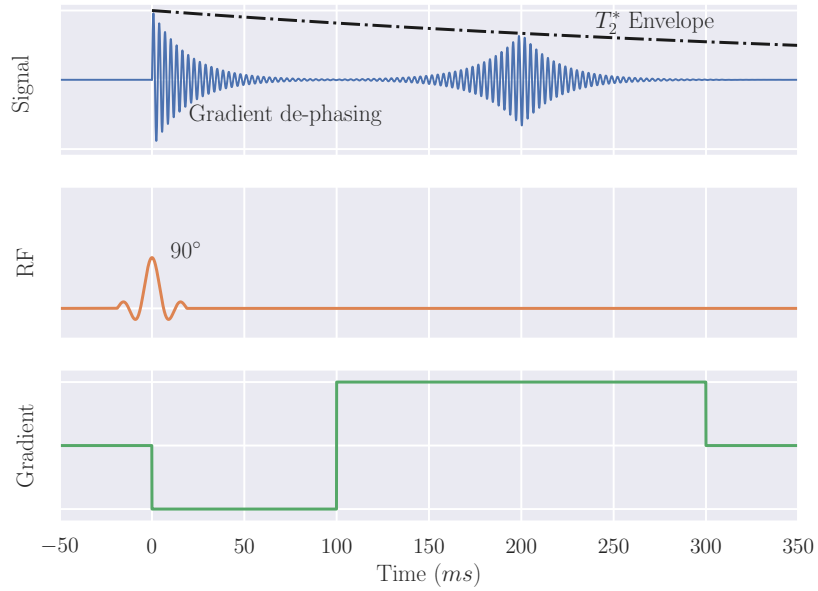


Figure 2.5: A schematic of a basic Gradient Echo (GE) sequence with TE 200 ms.

In reality, the gradients cannot switch polarity instantaneously due to the inductance of the gradient coils and characteristics of the amplifiers used to generate the gradients. This phenomenon leads to the gradient waveform being trapezoidal, however, to aid clarity in schematics within this chapter, an idealised gradient waveform has been shown. This characteristic of gradients is known as slew rate and is defined as the peak gradient amplitude upon the rise time, Figure 2.6, and for modern MRI scanners is of the order of 200 T/m/s.

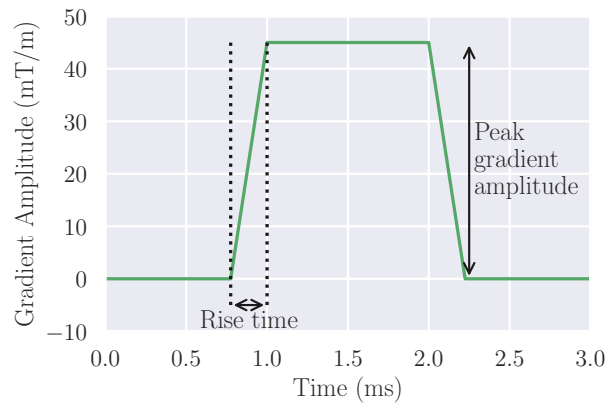


Figure 2.6: A gradient waveform with typical peak gradient amplitude, rise time and slew rate.

2.2.3 Dipole-Dipole Interactions

As outlined in 2.2.1 and 2.2.2, dipole-dipole interactions are a primary contributing factor to T_1 and T_2 times. The factors that dictate the strength of these interactions are the types of spin involved, the distance between them, the angle between them and their motion.

The strength of the interaction depends on the gyromagnetic ratio of the spins involved. The magnitude of an electrons gyromagnetic ratio is much greater than that of a proton ($-28025 \text{ MHz T}^{-1}$ and 43 MHz T^{-1} respectively [5]) and as such proton-electron interactions are much stronger than proton-proton interactions.

The strength of the interaction is inversely proportional to the sixth power of distance (seen in Equations (2.19) and (2.20)) and thus means that dipole-dipole interactions are only effective over a very short range. As such, the majority of interactions are intramolecular rather than intermolecular.

The z component of a magnetic field produced by a dipole, μ is given by Equation 2.18,

$$B_{\mu z} \propto \frac{\mu}{r^3} (3 \cos^2 \theta - 1) \quad (2.18)$$

producing the field shown in Figure 2.7. Here it can be seen that at certain angles, the magnetic field is zero, this occurs when $(3 \cos^2 \theta - 1) = 0$ and equates to angles at approximately 54.7° . These angles are known as magic angles. If the dipoles are orientated at approximately the magic angle to the B_0 field, their T_2 will be increased.

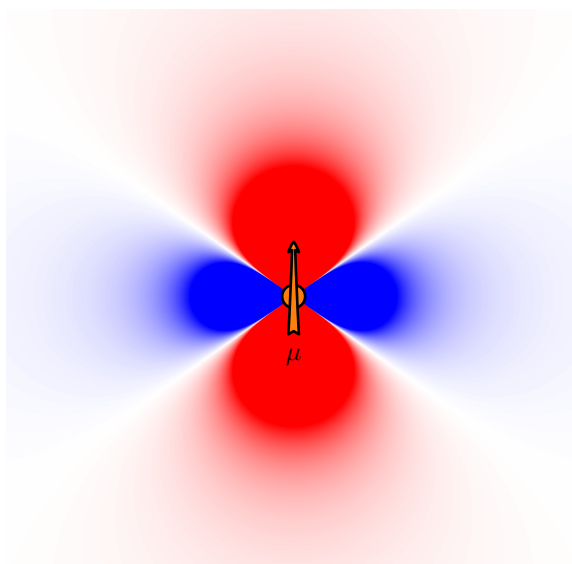


Figure 2.7: The z component of the magnetic field produced by dipole, μ .

Molecules can move in three different ways, translation, vibration and rotation. Translation has little effect on NMR signals as it is usually omnidirectional. Vibrational oscillations are at a much higher frequency than NMR phenomenon and as such do not affect the MRI signal. Rotations can be at similar frequencies to MRI and as such, influence T_1 and T_2 due to dipole-dipole interactions.

Each molecule in a sample will have a characteristic correlation time, τ_c , the time it takes the molecule to rotate by one radian. The correlation time is effected by how tightly bound the molecules are and their mass, light freely bound molecules like water in liquid form will have a short correlation time while heavy tightly bound molecules such as those found in bone, will have a longer correlation time. If a molecule is tumbling at a rate similar to the Larmor frequency, it will cause energy transfer to be more efficient, thus reducing T_1 . As the tumbling rate slows, the properties of the dipole become more similar to those of a static field, this means that nearby dipoles will experience magnetic fields perpetuated about B_0 and as such T_2 will decrease.

The mathematical framework of this phenomenon is given by the Solomon-

2.2. Relaxation and Contrast Mechanisms

Bloembergen equations [6] (Equations (2.19) and (2.20)). These equations predict T_1 and T_2 dependence on correlation time, Figure 2.8, where it can be observed that T_1 is lowest when the frequency of the molecular tumbling is similar to the Larmor frequency (labelled as τ_0 where $\tau_0 = 1/\omega_0$) and that T_2 decreases as correlation time increases. Tissues with a range of tumbling rates are highlighted in Figure 2.8; the molecules in Cerebrospinal Fluid (CSF) are weakly bound as they are in the liquid phase whereas solid tissues such as bone are tightly bound.

$$\frac{1}{T_1} = \frac{6}{20} \frac{\hbar^2 \gamma^4}{r^6} \left[\frac{\tau_c}{1 + \omega^2 \tau_c^2} + \frac{4\tau_c}{1 + 4\omega^2 \tau_c^2} \right] \quad (2.19)$$

$$\frac{1}{T_2} = \frac{3}{20} \frac{\hbar^2 \gamma^4}{r^6} \left[3\tau_c + \frac{5\tau_c}{1 + \omega^2 \tau_c^2} + \frac{2\tau_c}{1 + 4\omega^2 \tau_c^2} \right] \quad (2.20)$$

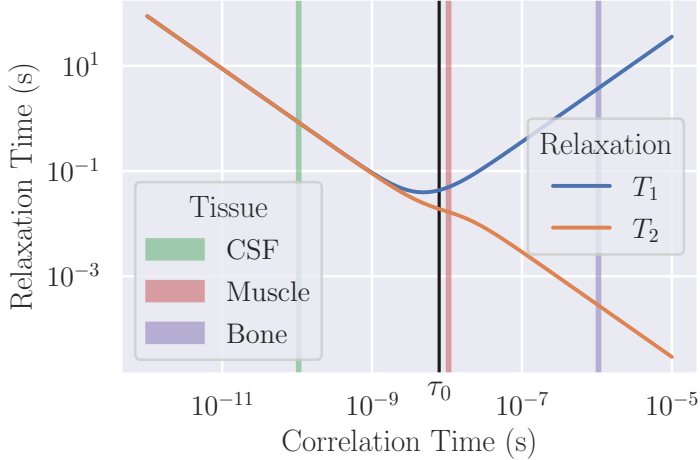


Figure 2.8: T_1 and T_2 dependence on molecular correlation time as predicted by the Solomon-Bloembergen equations. Tissues with a range of correlation times are highlighted.

2.2.4 Diffusion Imaging

Spins have been considered stationary until now, however, in biological tissues, they are often undergoing Brownian motion leading to diffusion. The

2.2. Relaxation and Contrast Mechanisms

signal from a sample can be made sensitive to the degree of diffusion taking place using diffusion gradients applied between excitation and echo. If a spin undergoes a translation while the gradient is being applied, it will be in a different magnetic field and thus at a different Larmor frequency while rephasing, resulting in additional signal attenuation. The degree of signal attenuation is proportional to the rate at which diffusion is occurring i.e. how far the spin has moved while the diffusion gradient was being applied. These diffusion gradients can either be bipolar, as seen in Figure 2.5 or monopolar if a SE sequence is used.

Not all diffusion is isotropic (occurs to the same degree in all directions), often the motion of the spins is restricted e.g. within tissue fibres. The amount of restriction is known as the fractional anisotropy where 0 represents isotropic diffusion e.g. a large vial of water, and 1 represents diffusion being constrained to a single dimension. By applying the diffusion gradients in different directions (and strengths) the preferred direction of diffusion and fractional anisotropy can be calculated. These techniques are used in Chapter 6.

2.2.5 Optimisation of Tissue Contrast

Quantitative mapping of T_1 , T_2 and T_2^* can often be a slow process due to the number of acquisitions required at different time points to sample relaxation curves. Often it is more desirable to acquire a volume at a single time with the intensity difference between tissues of interest maximised. Although the voxel intensities do not directly represent any quantitative underlying physical properties of the tissue, the contrast between tissues is sufficient for diagnosis or further analysis.

2.2. Relaxation and Contrast Mechanisms

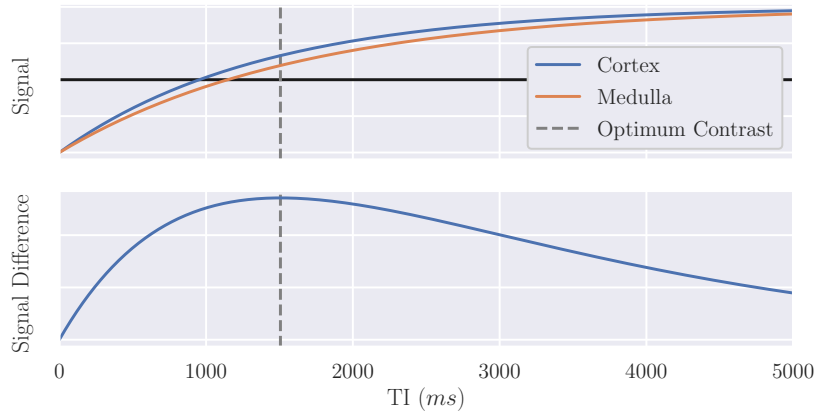


Figure 2.9: The signal generated from renal cortical and medullary tissues [7] and difference between signals. This shows that the contrast between the two tissues is optimal if the Inversion Time (TI) is 1500 ms.

2.3 Forming an Image

2.3.1 Signal Localisation

So far, NMR has been applied to measure signals from the entire sample, gaining no information about the spatial variation within it. MRI applies the techniques of NMR to spatially resolve the location of the signal.

The key concepts of MRI were developed by multiple groups in the 1970s. Lauterbur used magnetic field gradients and a back-projection reconstruction technique to generate 2D images in 1978 [8]. Simultaneously Mansfield was working on “NMR diffraction” introducing the mathematical framework of reciprocal k -space [9] and later slice selective excitation [10]. The final key insight was provided by Ernst who published the first Fourier imaging method [11], this used non-selective excitations and linear gradients to generate 2D Fourier encoded images. These techniques are still the basis of MRI today.

The concepts of signal localisation will be introduced through the example of an axial acquisition, Figure 2.10

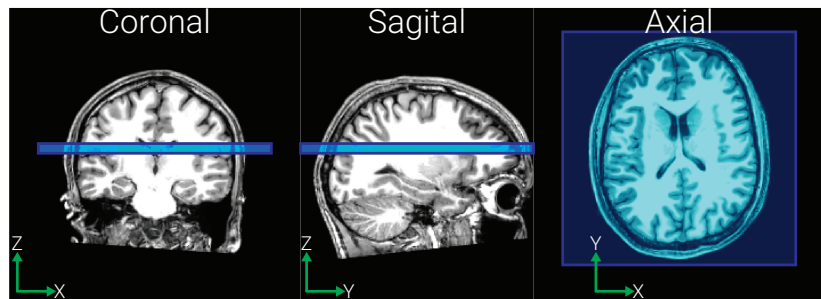


Figure 2.10: Planning used in the signal localisation example.

Gradient Fields

Signal localisation makes use of gradient fields. These produce small linear perturbations in B_0 and are applied in a combination of the x , y and z direction to enable arbitrary gradient directions and result in B_0 varying with position,

2.3. Forming an Image

\mathbf{r} ,

$$B_z(r) = (B_0 + \mathbf{G} \cdot \mathbf{r}) \hat{k}. \quad (2.21)$$

As such, the resonant frequency of the spins can also be described as a function of position and, because the gradients are not static, time,

$$\omega(x, y, z, t) = \gamma (B_0 + G_x(t)x + G_y(t)y + G_z(t)z) \quad (2.22)$$

Slice Selection

The initial step in localisation is to measure the signal from a single, spatially defined, slice. If a gradient is applied along the z direction, G_z , the magnetic field experienced by the spins at position z will be

$$B(z) = B_0 + G_z z. \quad (2.23)$$

As such, from the simplification of (2.22), the Larmor frequency becomes

$$\omega(z) = \gamma (B_0 + G_z z). \quad (2.24)$$

If a frequency selective RF pulse is applied to the sample, it will only excite spins within the corresponding bandwidth and thus only a slice of desired thickness. This slice-selective thickness, Δz , can be changed by either adjusting G_z or the bandwidth of the excitation pulse, $\Delta\omega$.

$$\Delta z = \frac{\Delta\omega}{\gamma G_z} \quad (2.25)$$

The excitation profile achieved by a slice selective pulse can be approximated by a Fourier transform. Generally, a rectangular slice profile is wanted and as such, the RF pulse takes the form of a sinc function. To achieve a perfect rectangular pulse, the sinc would have to be infinite in length. Given the lack of infinite time available during an MRI examination, a truncated sinc pulse is used, generally including three or five lobes and a Gaussian filter.

2.3. Forming an Image

The gradient applied will result in de-phasing of the spins as in a GE sequence, therefore a gradient of the opposite polarity and half the magnitude is applied after the RF pulse to re-phase the spins, Figure 2.11a.

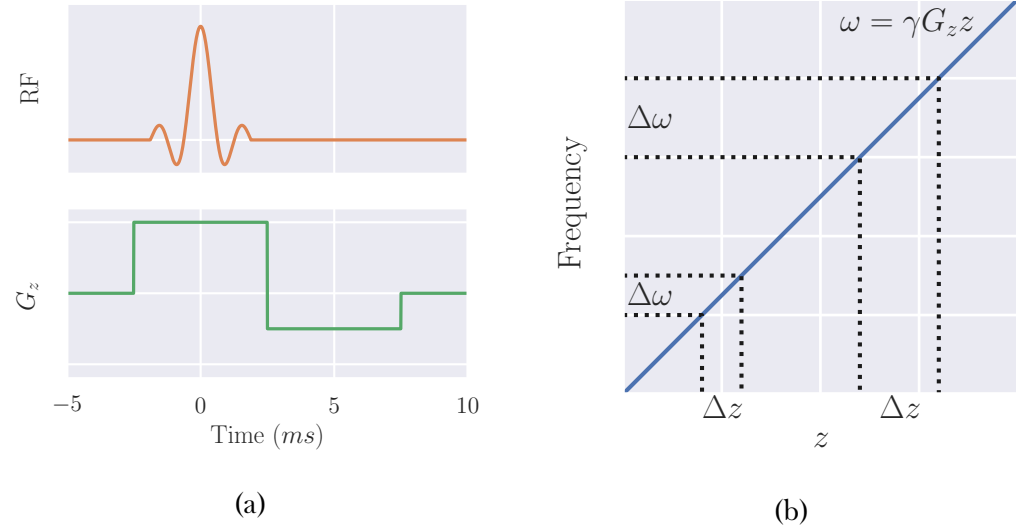


Figure 2.11: (a) A truncated sinc pulse of bandwidth $\Delta\omega$ being applied over a slice selective gradient followed by the negative re-phasing gradient lobe. Note that the area under the re-phasing gradient is half of that of the slice selective gradient. (b) Example slices of thickness Δz being excited by RF pulses of bandwidth $\Delta\omega$ showing that excitation pulses of larger bandwidth result in thicker slice profiles.

Phase Encoding

The signal has been localised from a full 3D volume to a defined 2D volumetric slice. To localise the signal in the next dimension, phase encoding is used. This technique uses a gradient in the y direction applied for time T . For the duration of G_y the spins precess with a frequency according to their position in the y direction

$$\omega(y) = \gamma(B_0 + G_y y), \quad (2.26)$$

2.3. Forming an Image

and as such accrue a phase shift relative to if no gradient was applied, given by

$$\phi(y) = \gamma y \int_0^T G_y(t) dt. \quad (2.27)$$

Acquisitions must be repeated with different amplitudes/durations of G_y to fully sample in the y direction, Figure 2.13.

Phase aliasing occurs because the whole sample produces signal, whether it is in the Field Of View (FOV) or not. As there is a finite range of phase values (0 to 2π) tissue outside the FOV can have the same value as tissue within the FOV this results in the two signals becoming indistinguishable and therefore combined in a process known as wrapping. This artefact is illustrated in Figure 2.12.

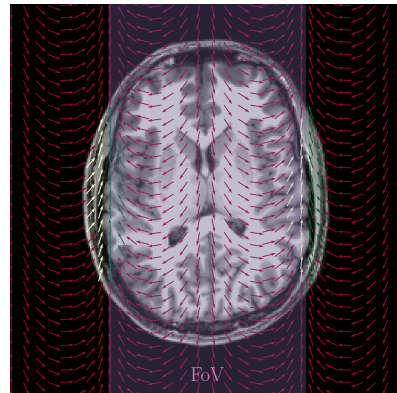


Figure 2.12: Spins outside the FOV have the same phase value as those within the FOV and thus wrapping occurs.

Frequency Encoding

Finally, the signal needs to be localised in the x direction. This is achieved using frequency encoding. Here the gradient, G_x is applied during the acquisition section of the sequence i.e. when the signal is being sampled. As the gradient is being applied during readout, those spins in the centre of the gradient (at field B_0) will be precessing at the Larmor frequency while those in a stronger or weaker field will be precessing faster or slower respectively. By sampling the signal generated and applying a Fourier transform to separ-

2.3. Forming an Image

ate components of the signal at each frequency, the signal is spatially resolved in all three dimensions. An overview of a basic signal localisation scheme is shown in Figure 2.13.

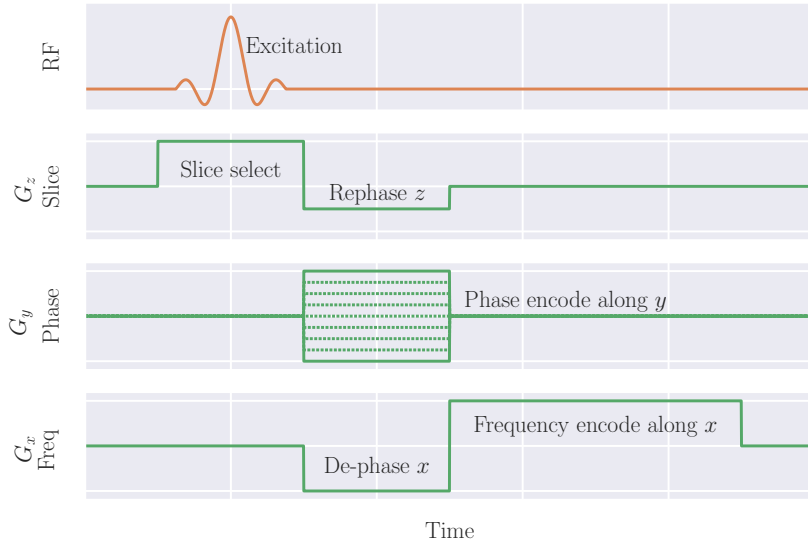


Figure 2.13: A basic spacial localisation pulse sequence showing how gradients applied along the z , y and x directions can be used to localise the signal in the corresponding dimensions.

k -space

k -space, sometimes known as Fourier space, is a useful concept for interpreting MRI pulse sequences and represents the spatial frequencies of the image. Immediately after an excitation pulse and rewind gradient, the signal being sampled is at the origin of k -space, corresponding to low spatial frequencies, or the low resolution aspects of the image e.g. which voxels are inside or outside the body. As gradients are applied to the sample, sampling moves out from the centre of k -space to higher spatial frequencies corresponding to finer detail within the image. For a 2D acquisition, as above, the location in k -space is defined by (2.28) and (2.29) where G_x and G_y are the gradients in the frequency encode and phase encode directions respectively

2.3. Forming an Image

and t_x and t_y are the duration the gradient is applied for.

$$k_x = \gamma G_x t_x \quad (2.28)$$

$$k_y = \gamma G_y t_y \quad (2.29)$$

When recording MRI data, the continuous signal must be discretised. The higher the sampling frequency i.e. the closer together in k -space the samples are, Δk , the wider the FOV and the further out from the origin of k -space are samples, the higher resolution the image will be. Examples of k -space sampling patterns and their corresponding image are shown in Figure 2.14.

From k -space to Image Space

The raw data sampled in k -space can be reconstructed to an image via a Fourier transform. When the quadrature data undergoes a 2D Fourier transform, it produces a complex image composed of a real and imaginary part. These constituent parts of the image can be converted into magnitude and phase images with the magnitude representing the spin density.

Coordinate Systems

The above example was chosen so that only one gradient is used at once however if the planning of the acquisition is more complicated, the nomenclature can become more confusing, as such, for clarity multiple coordinate systems are often used.

Scanner Space This coordinate system has its origin at isocentre of the scanner and is defined in terms of x , y and z .

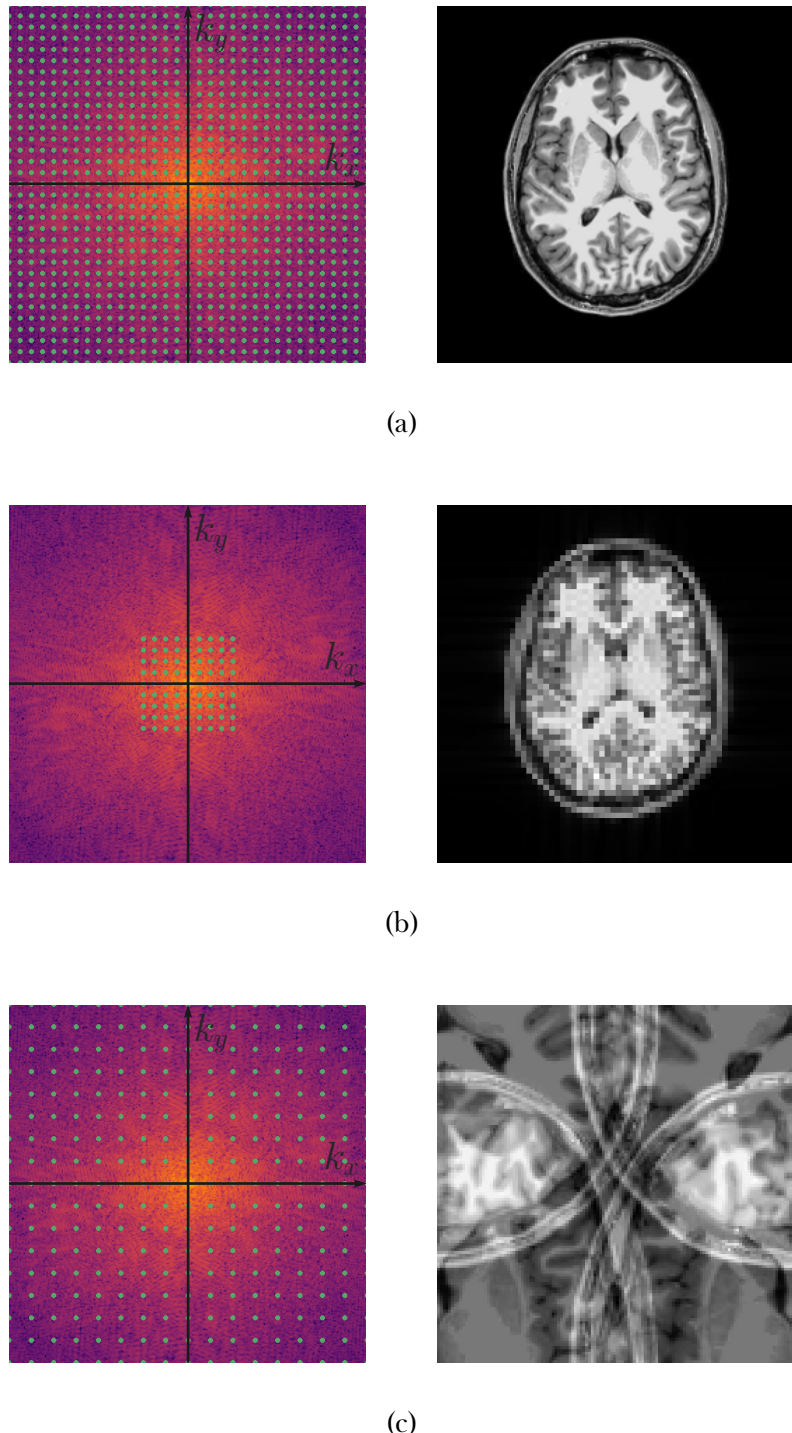


Figure 2.14: (a) Fully samples k -space and the corresponding image. (b) Centre sampling of k -space produces a lower resolution image. (c) Sampling with a larger Δk resulting in a decreased FOV and aliasing.

Imaging Space The coordinates of this system are defined by the directions used in signal localisation, M for the frequency encode direction (also called magnitude), P for the phase encode direction and S for the slice select direc-

2.3. Forming an Image

tion.

Anatomical Space Defined in terms of the subjects orientation in the scanner, this coordinate system has the axis, Right-Left (R-L), Anterior-Posterior (A-P) and Superior-Inferior (S-I).

2.3.2 Image Acquisition Acceleration

One of the recurring limiting factors in MRI is the acquisition time. For neuroimaging applications the relatively slow acquisition of MRI limits subject throughput or the number of different measures that can be performed. In abdominal imaging, acquisition times can be even more of a hindrance given many scans are performed while the subject is holding their breath on expiration. As such, image acquisition acceleration techniques have been developed. These techniques sacrifice a small amount of Signal to Noise Ratio (SNR) for a decrease in acquisition time.

Partial Fourier

Fully sampled k -space contains inherent redundancy as it contains its own complex conjugate; the real components of the signal are symmetric while the imaginary components are anti-symmetric. This means that no contrast information is lost if a reduced area of k -space is sampled e.g. only sample 66% of k -space. This technique does impact phase information though so should not be used in acquisitions where downstream processing requires accurate phase. Known as partial Fourier or half-scan, this technique results in a decreased SNR and can introduce image artefacts as the partial Fourier factor approaches 50%, however, the acquisition time reduces by approximately the percentage of k -space sampled e.g. an acquisition that would take three minutes fully sampled will take two minutes if a partial Fourier factor of 66% is used. An example of reconstructions of 100%, 75% and 51% of k -space

2.3. Forming an Image

are shown in Figure 2.15

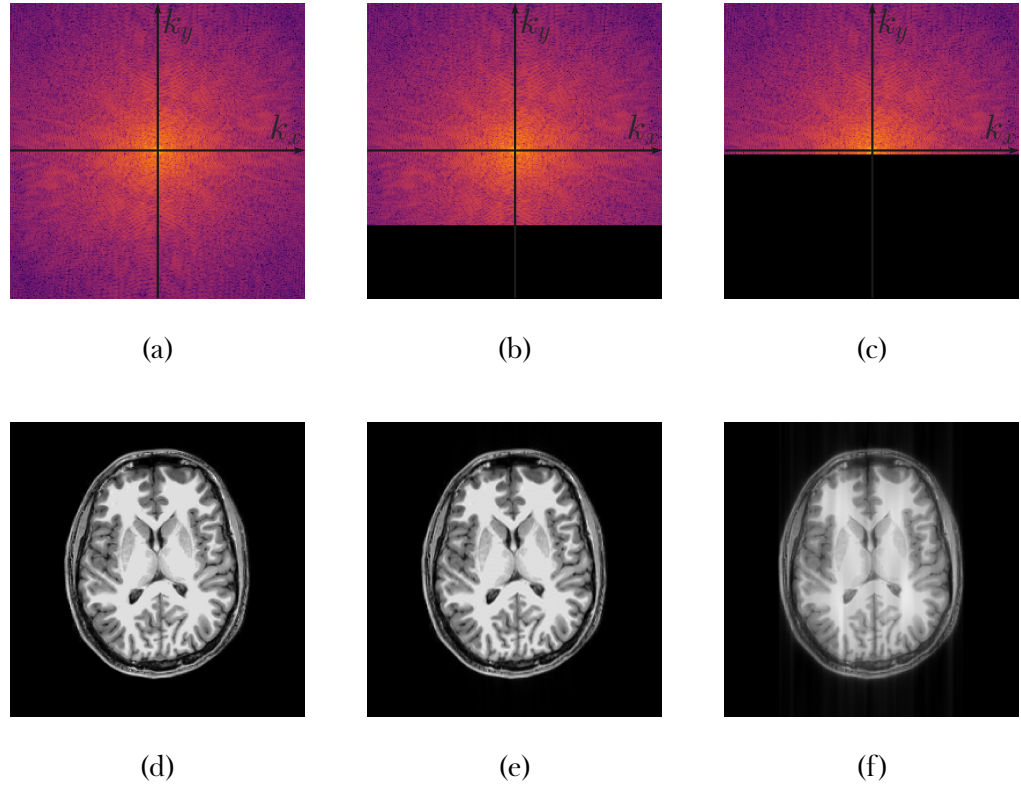


Figure 2.15: Full, (a), 75%, (b), and 51%, (c), k -space sampling and their corresponding reconstructions in image space, (d), (e) and (f) respectively.

Sensitivity Encoding (SENSE)

Most modern scanners use different coils for RF transmission, and signal receiving. The transmission coil is usually built into the bore of the magnet while the receive coil is placed as close to the source of the signal as possible. These receive coils are usually composed of multiple smaller coils to make an array, each with its own signal sampling hardware. This means that it is possible to record signal from multiple coils simultaneously with different coils supplying data for each line of k -space e.g if the array has two coils, one coil will record the odd lines of k -space and the other, the even lines, thus resulting in an increase in acquisition speed [12]. This parallel sampling technique reduces the lines of k -space sampled per coil and results in wrapping as seen in Figure 2.14c, albeit only in the phase direction. To combat this, the spatial

2.3. Forming an Image

sensitivity profile of each element within the array i.e. the area it can measure signal from, is measured. Using this prior knowledge of signal locations, each coil elements data can be unwrapped before the data from all elements is combined into a single volume.

The Sensitivity Encoding (SENSE) factor is the degree to which k -space is under-sampled and is limited to the number of elements in the receive array. Applying higher SENSE factors increases acquisition speeds, however, reduces SNR.

2.3.3 Image Acquisition Schemes

Many different acquisition schemes have been developed for sampling k -space. Outlined below are some of the key sequences that form the basis of much of MRI.

Spin Warp Imaging

The simplest uniformly sampled k -space trajectory is spin warp imaging. This technique is based on the GE scheme and samples one line of k -space per excitation, or shot, a schematic is shown in Figure 2.16. Each shot applies a different phase encode gradient to move a different amount in the k_y direction. The signal is then sampled while a gradient is applied in the frequency direction, also known as the readout gradient. The acquisition time for this sequence is very long because it only collects one line of k -space per shot and as such this technique is sensitive to subject motion.

2.3. Forming an Image

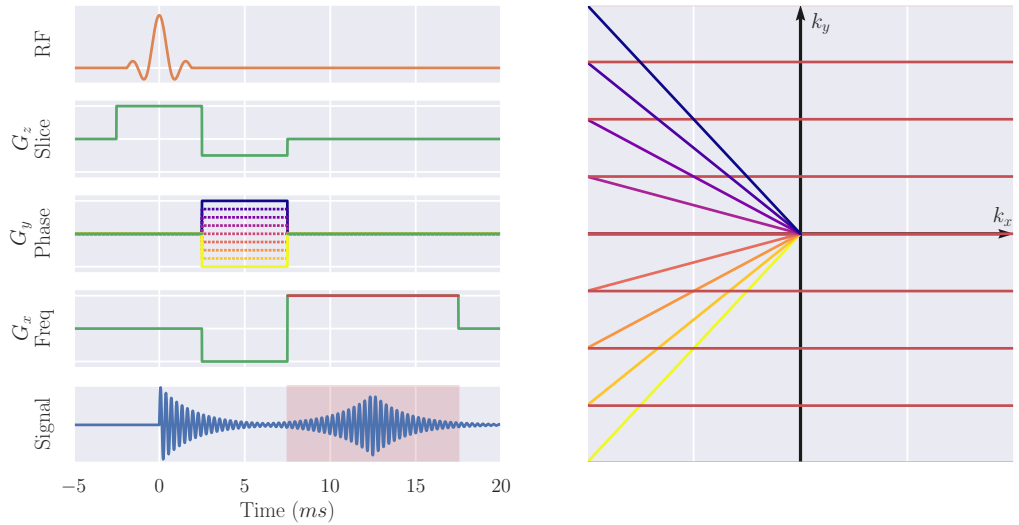


Figure 2.16: A schematic of the spin warp image sequence. The Pulse Sequence Diagram (PSD) shows the different phase encoding gradients, G_y , in colours from yellow to purple and the readout gradient, G_x , in red. These colours correlate with the colours in the k -space trajectory. The signal recorded is highlighted in red.

Echo Planar Imaging (EPI)

A much faster technique than spin warp imaging is Echo Planar Imaging (EPI) [9]. This technique samples all lines of k -space in a single excitation shot with an acquisition time typically less than 100 ms. The Pulse Sequence Diagram (PSD) and k -space trajectory for this sequence are shown in Figure 2.17. The sequence begins very similarly to the spin warp sequence with a slice selective excitation and an acquisition of the bottom line of k -space, however, instead of a spoiler followed by another excitation as in spin warp imaging, in EPI a small positive phase encode gradient ‘blip’ is applied to move up a line in k -space, followed by an inversion of the readout gradient polarity. This blip followed by reversed readout is repeated, zig-zagging up k -space until the desired k -space is sampled.

2.3. Forming an Image

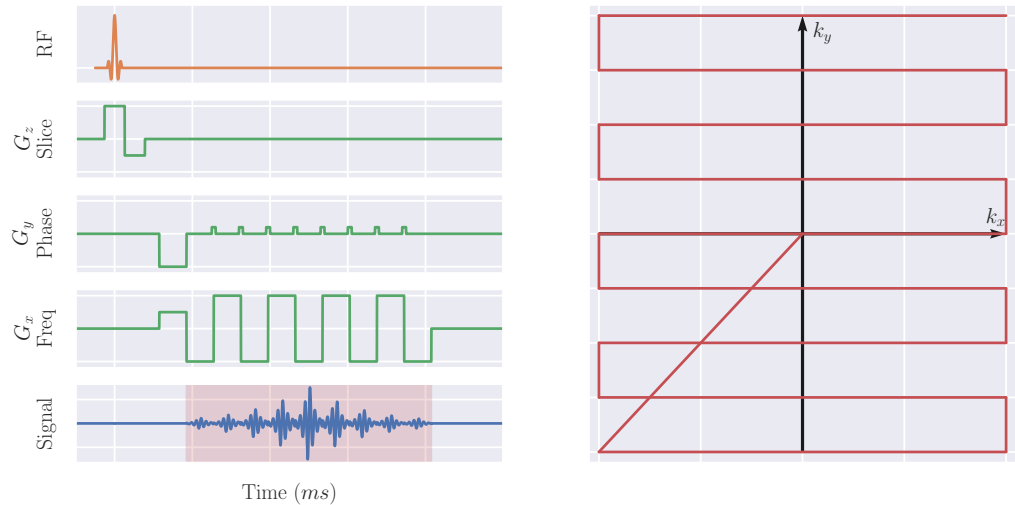


Figure 2.17: A schematic of the EPI pulse sequence and k -space trajectory.
Not this diagram is not to scale.

While this sequence has a very quick acquisition time, it does have drawbacks. The long train of echoes makes EPI more sensitive to inhomogeneities in the B_0 field caused by different tissue susceptibilities or poor shimming. Eddy currents and imperfections in gradient coils cause small differences in lines collected in the positive and negative direction, leading to a Nyquist ghost artefact. Eddy currents induced by the phase encode blips also cause geometric distortions in the image, Figure 2.18, however, these can be corrected via post processing if an image with phase encode blips of opposite polarity is collected i.e. collect images sampling k -space from both bottom to top and top to bottom.

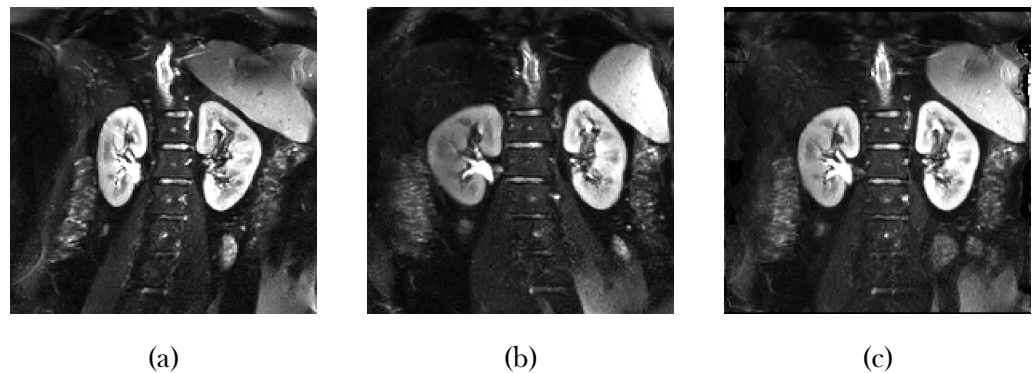


Figure 2.18: Geometric distortions in EPI when phase encode blips are (a) positive, (b) negative and (c) corrected via post processing.

2.3. Forming an Image

Turbo Spin Echo (TSE)

The Turbo Spin Echo (TSE) sequence, also known as Fast Spin Echo (FSE) or Rapid Acquisition with Relaxation Enhancement (RARE), is an expansion on the conventional SE sequence applying evenly spaced 180° RF refocusing pulses to generate multiple echo from a single excitation, these echoes are used to record multiple lines of k -space. The number of echoes is known as the Echo Train Length (ETL), or ‘turbo factor’ and is the factor by which the scan time is reduced compared to a conventional spin echo sequence and is usually between 2 and 30 per TR; the time between echoes is known as the echo spacing and is typically 15 - 25 ms.

Each line of k -space is acquired at a different time after excitation, as such, they will have different T_2 weightings, it is therefore important to ensure the centre of k -space is acquired at the desired TE as this echo will dominate the image contrast. The time between excitation and the centre of k -space is known as the Effective Echo Time (eTE).

The decrease in acquisition time comes at the expense of RF exposure, the large number of 180° pulses leads to lots of energy in the form of heat being deposited in the tissue being imaged, this is known as Specific Absorption Rate (SAR). SAR limits are imposed when scanning to avoid damaging any tissue and as such TSE with its high RF power can easily exceed these limits. Modern TSE sequences can reduce the angle of the refocusing pulse, however this can come at the expense of quantitative accuracy.

2.3. Forming an Image

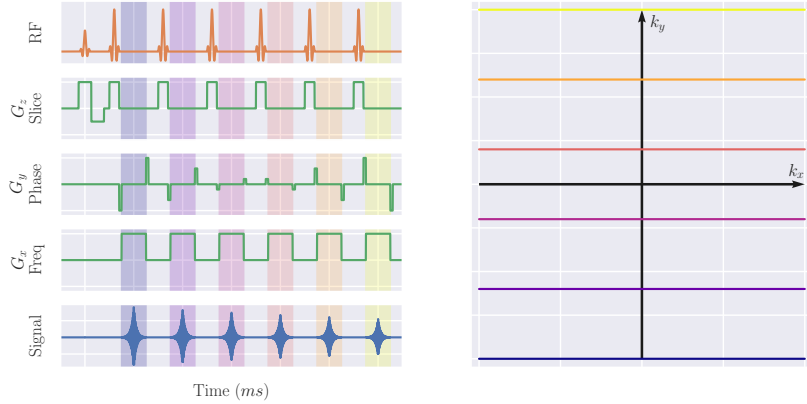


Figure 2.19: A schematic of the TSE pulse sequence and k -space trajectory. The coloured bands on the PSD correspond to the colours of the k -space trajectories. Note this diagram is not to scale.

Half-Fourier Single-shot Turbo spin Echo (HASTE)

The Half-Fourier Single-shot Turbo spin Echo (HASTE) sequence uses a combination of the techniques above. A single excitation is followed by a very long echo train with short echo spacing. This allows a large proportion of k -space to be sampled within a single TR and thus a whole slice is acquired. To minimise the number of lines of k -space acquired and thus the ETL, partial Fourier techniques are utilised. The relatively long TE required for a HASTE sequence means images are normally T_2 weighted.

The advantage of HASTE is its rapid acquisition. It can be used to minimise the effects of motion when scanning uncooperative patients, fetuses or structures the subject has no control over such as the bowel. Alternatively it can be used to capture a large FOV in a single breath hold, thus minimising the effects of inconsistent expiration level, as in Chapter 5. The very long ETL can cause significant blurring of the image, thus reducing its clinical readability.

Turbo Field Echo (TFE)

Turbo Field Echo (TFE), also known as ulatrafast GE, is designed to speed up acquisition of GE images by reducing the TR between excitations. Typical basic GE sequences have relatively long TR to allow the recovery of longitudinal magnetisation. The flip angle used in the TFE sequence is much smaller than the examples explored so far, usually approximately 10° thus leaving a large component of the magnetisation in the longitudinal direction while tipping enough magnetisation into the transverse plane to record a signal at an acceptable SNR. Between each excitation, the transverse magnetisation is spoiled to ensure the images are only T_1 weighted.

After a train of equally spaced RF pulses of Flip Angle (FA), α , and period, TR, the longitudinal magnetisation reaches a steady state, S_{TFE} , after a sufficient number of pulses. This steady state signal depends on the T_1 of the tissue and the FA and TR of the sequence. Assuming perfect transverse magnetisation spoiling between each RF pulse, this equilibrium signal is given by,

$$S_{TFE} = M_0 \frac{\sin(\alpha) [1 - \exp(-TR/T_1)]}{1 - \cos(\alpha) \exp(-TR/T_1)} \exp\left(-\frac{TE}{T_2^*}\right). \quad (2.30)$$

The angle that produces the maximum signal, known as the Ernst angle, α_E , is given by,

$$\alpha_E = \arccos \left[\exp\left(-\frac{TR}{T_1}\right) \right]. \quad (2.31)$$

Figure 2.20 shows the ratio of the steady state signal to the fully recovered, 90° excitation signal of renal cortex (T_1 of 1376 ms) for a range of flip angles and TR. Additionally the Ernst angle is shown.

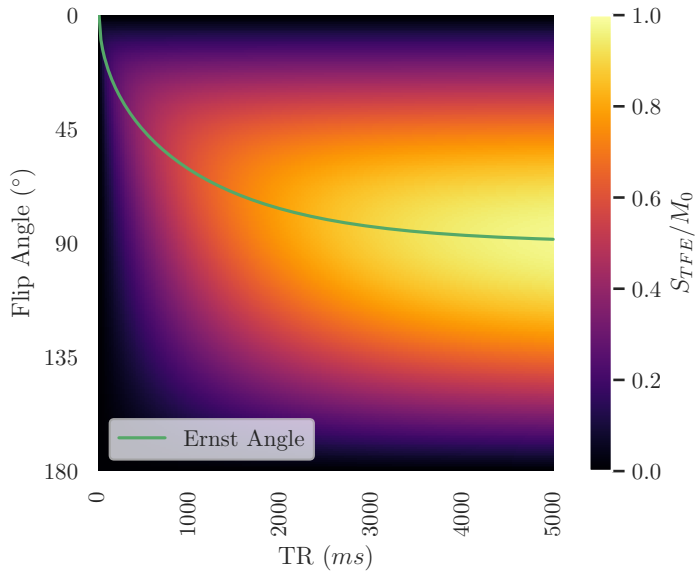


Figure 2.20: The expected steady state signal of a TFE pulse sequence and Ernst angle when imaging renal cortex.

2.4 Conclusion

This chapter has introduced the basic concepts of NMR and MRI required for interpreting this thesis. These techniques are built upon in the experimental chapters for quantification of renal properties, both in-vivo and ex-vivo.

2.5 References

1. Harris, R. K. N.m.r. and the Periodic Table. *Chemical Society Reviews* **5**, 1–22. ISSN: 1460-4744 (1st Jan. 1976).
2. Bernstein, M. A., King, K. F. & Zhou, X. J. *Handbook of MRI Pulse Sequences* 1041 pp. ISBN: 978-0-08-053812-4. Google Books: d6PLHcyejEIC (Elsevier, 21st Sept. 2004).
3. Westbrook, C. *MRI at a Glance* 138 pp. ISBN: 978-1-119-05354-5. Google Books: WeRbCwAAQBAJ (John Wiley & Sons, 18th Nov. 2015).
4. Bloch, F. Nuclear Induction. *Physical Review* **70**, 460–474 (1st Oct. 1946).
5. Mohr, P. J., Newell, D. B. & Taylor, B. N. CODATA Recommended Values of the Fundamental Physical Constants: 2014. *Reviews of Modern Physics* **88**, 035009 (26th Sept. 2016).
6. Solomon, I. Relaxation Processes in a System of Two Spins. *Physical Review* **99**, 559–565 (15th July 1955).
7. Cox, E. F. *et al.* Multiparametric Renal Magnetic Resonance Imaging: Validation, Interventions, and Alterations in Chronic Kidney Disease. *Frontiers in Physiology* **8**. ISSN: 1664-042X (2017).
8. Lauterbur, P. C. Image Formation by Induced Local Interactions: Examples Employing Nuclear Magnetic Resonance. *Nature* **242**, 190–191. ISSN: 1476-4687 (5394 Mar. 1973).
9. Mansfield, P. & Grannell, P. K. NMR "Diffraction" in Solids? *Journal of Physics C: Solid State Physics* **6**, L422–L426. ISSN: 0022-3719 (Nov. 1973).
10. Garboway, A. N., Grannell, P. K. & Mansfield, P. Image Formation in NMR by a Selective Irradiative Process. *Journal of Physics C: Solid State Physics* **7**, L457–L462. ISSN: 0022-3719 (Dec. 1974).
11. Kumar, A., Welti, D. & Ernst, R. R. NMR Fourier Zeugmatography. *Journal of Magnetic Resonance (1969)* **18**, 69–83. ISSN: 0022-2364 (1st Apr. 1975).

2.5. References

12. Pruessmann, K. P., Weiger, M., Scheidegger, M. B. & Boesiger, P. SENSE: Sensitivity Encoding for Fast MRI. *Magnetic Resonance in Medicine* **42**, 952–962. issn: 1522-2594 (1999).